The Final Fates of Close Hot Subdwarf–White Dwarf Binaries: Mergers Involving He/C/O White Dwarfs and the Formation of Unusual Giant Stars with C/O-Dominated Envelopes

Josiah Schwab[1] and Evan B. Bauer[2]

[1] Department of Astronomy and Astrophysics, University of California, Santa Cruz, CA 95064, USA; jwschwab@ucsc.edu
[2] Center for Astrophysics | Harvard & Smithsonian, 60 Garden Street, Cambridge, MA 02138, USA
Received 2021 July 2; revised 2021 August 3; accepted 2021 August 5; published 2021 October 21

Abstract

Recently, a class of Roche-lobe-filling binary systems consisting of hot subdwarf stars and white dwarfs (WDs) with sub-hour periods has been discovered. At present, the hot subdwarf is in a shell He-burning phase and is transferring some of its remaining thin H envelope to its WD companion. As the evolution of the hot subdwarf continues, it is expected to detach, leaving behind a low-mass C/O-core WD secondary with a thick He layer. Then, on a timescale of ~ 10 Myr, gravitational wave radiation will again bring the systems into contact. If the mass transfer is unstable and results in a merger and a catastrophic thermonuclear explosion is not triggered, it creates a remnant with a C/O-dominated envelope, but one still rich enough in He to support an R Corona Borealis-like shell-burning phase. We present evolutionary calculations of this phase and discuss its potential impact on the cooling of the remnant WD.

Unified Astronomy Thesaurus concepts: White dwarf stars (1799); Subdwarf stars (2054); Stellar mergers (2157); R Coronae Borealis variable stars (1327)

1. Introduction

Recently, Kupfer et al. (2020a, 2020b) described a new class of binaries consisting of a Roche-lobe-filling hot subdwarf transferring mass to a white dwarf (WD) companion. The first of these objects, ZTF J213056.71+442046.5 (hereafter ZTF J2130+4420), is the most compact hot subdwarf binary currently known with a period of $P = 39.34$ minutes. Modeling of the system yields a low-mass hot subdwarf donor with a mass $M_{\rm sdOB} = 0.337 \pm 0.015\, M_\odot$ and a WD accretor with a mass $M_{\rm WD} = 0.545 \pm 0.020\, M_\odot$. The second of these objects, ZTF J205515.98+465106.5 (hereafter ZTF J2055 +4651), has a period of $P = 56.35$ minutes. Modeling of the system yields an He-sdOB mass of $M_{\rm sdOB} = 0.41 \pm 0.04\, M_\odot$ and a WD mass of $M_{\rm WD} = 0.68 \pm 0.05\, M_\odot$. The timescales for these systems to merge (as WD–WD binaries) are ≈ 17 and ≈ 30 Myr, respectively.

Similar binaries may realize a variety of final fates, depending on the masses of the component objects and their post-common-envelope orbital period. Bauer & Kupfer (2021) systematically map out the phases of mass transfer in these systems, which can involve stable mass transfer of both H- and He-rich material. This can lead to outcomes including the formation of an AM CVn system or the accumulation of a thick He shell and the destruction of the system through a thermonuclear double detonation (e.g., Neunteufel et al. 2016, 2019; Bauer et al. 2017). Alternatively, the subdwarf donor may detach, leading to the formation of a double WD binary with a C/O primary WD and low-mass hybrid He/C/O WD. Zenati et al. (2019) describe the formation and evolution of hybrid He/C/O WDs and characterize their properties and birth rates.

Gravitational wave radiation will again bring the systems into contact. The stability of the resulting mass transfer depends on the spin–orbit coupling in the binary (e.g., Marsh et al. 2004) and the dissipative influence of material ejected in potential novae (Shen 2015). It is plausible that a significant fraction of the systems experience unstable mass transfer and merge. As discussed by Zenati et al. (2019), the significant He

content of the He/C/O hybrid WD could have an important role in the WD–WD merger. In particular, the He-rich secondary again offers the possibility of a double-detonation thermonuclear explosion. However, given the relatively low mass of the primary C/O WD in the prototype systems ($\lesssim 0.7\, M_\odot$), this outcome seems unlikely (e.g., Shen et al. 2018). If the merger does not lead to a catastrophic explosion, it produces a remnant that will eventually become a single massive WD.

In this paper, we illustrate this pathway by building a simple model of the post-merger state and following its evolution. Because of the significant amount of He present on the secondary WD, the merger remnant first sets up a stable He-burning shell and spends $\sim 10^5$ yr as a He-shell-burning giant. Once the He finishes burning and/or is lost to stellar winds, the remnant contracts to a compact configuration and then moves down the cooling track as a massive WD. Because of its merger origin, the composition profile can be different than that of a WD from single star evolution, and we discuss how this can affect the WD cooling through the production of ^{22}Ne.

A closely related scenario is the merger of a He-core WD with a low-mass C/O-core WD. This is thought to produce the R Coronae Borealis (RCB) stars (e.g., Webbink 1984; Clayton 2012) and extreme He (EHe) stars (e.g., Saio & Jeffery 2002; Jeffery 2008). As we outline the evolution, we compare and contrast with these objects. The observed sample of RCB stars, with their measured surface abundances (e.g., Asplund et al. 2000; Clayton et al. 2007), motivates detailed studies of their evolution including particular attention to the nucleosynthesis (e.g., Menon et al. 2013; Zhang et al. 2014; Munson et al. 2021). The calculations we present here are more schematic than the state-of-the-art RCB models. The goal of this work is to consider a variation on the basic Webbink (1984) scenario, in which the He-core WD secondary is instead a low-mass C/O-core WD with a thick He layer, and illustrate that this may produce an unusual object akin to, but distinct from, the RCB stars.

2. Evolution to a Single WD

2.1. Initial Post-merger Model

Hydrodynamic simulations of double WD mergers show that immediately after the merger (i.e., a few orbital periods after the tidal disruption of the secondary WD), the merger remnant can be divided into three main regions: the cold core of the primary, a hot shock-heated envelope at the primary/secondary interface, and a rotationally supported disk of material from the secondary (Dan et al. 2014). Then, efficient angular momentum transport due to magnetohydrodynamic processes internally redistributes angular momentum on timescales much shorter than the thermal timescale of the remnant (Schwab et al. 2012; Shen et al. 2012). The remnant becomes primarily thermally supported and approaches a quasi-spherical state allowing its further evolution to be treated as a stellar evolution problem.

We construct and evolve stellar models using MESA r12778 (Paxton et al. 2011, 2013, 2015, 2018, 2019). The initial merger model generation procedure is similar to that described in Schwab (2021). First, a high-entropy, pure-helium model of the desired mass is constructed. Next, its composition and temperature/entropy profiles are slowly altered to match specified target profiles (described subsequently). This model then forms the starting condition and is allowed to evolve without further intervention. The technical details of this procedure are irrelevant given the illustrative nature of the calculation presented here, but the Modules for Experiments in Stellar Astrophysics (MESA) input files are available on Zenodo: 10.5281/zenodo.5063047.

We generate an initial condition that resembles a possible outcome from the future evolution of ZTF J2130+4420 under the constraint that the pre-merger component masses are among the set of Dan et al. (2014) WD–WD merger simulations. Therefore, we model a $0.35 \, M_\odot$ C/O-core WD with a thick He layer merging with a $0.55 \, M_\odot$ C/O WD. In the Dan et al. (2014) simulation with this total mass and mass ratio, they find $M_{\rm core} \approx 0.4 \, M_\odot$, $M_{\rm env} \approx 0.3 \, M_\odot$, and $M_{\rm disk} \approx 0.2 \, M_\odot$. (In this case, the Dan et al. (2014) secondary was a He WD, but they demonstrate that these quantities depend primarily on the mass ratio).

We assign the core a cold temperature of 5×10^7 K. The peak temperature is $T_{\rm peak} \approx 2 \times 10^8$ K and we choose a constant entropy for the envelope material that yields this temperature. The choice of the envelope entropy will affect the early evolution, but after a thermal time, the entropy of the outer layers is reset by the luminosity from below. Our model is nonrotating.

In order to set the composition, we rely on a model of an $\approx 0.6 \, M_\odot$ C/O WD primary generated from a $3.1 \, M_\odot$ single star and the $\approx 0.36 \, M_\odot$ WD secondary evolved from the He-sdO model presented in Kupfer et al. (2020a). In evolving the He-sdO model into the WD stage, much of the H in the envelope burns away to form a much thinner envelope than the $0.01 \, M_\odot$ envelope in the He-sdO phase presented in Kupfer et al. (2020a). The resulting secondary WD envelope has a total H mass of $\approx 8 \times 10^{-4} \, M_\odot$.

In the core region, we set the composition to be the averaged mass fractions of the core of the primary WD. In the envelope/disk region, we use a set of averaged mass fractions that reflects the result of uniformly mixing the outer $\approx 0.15 \, M_\odot$ of the primary WD and the entire secondary WD. The composition transitions between these over a small blend region located
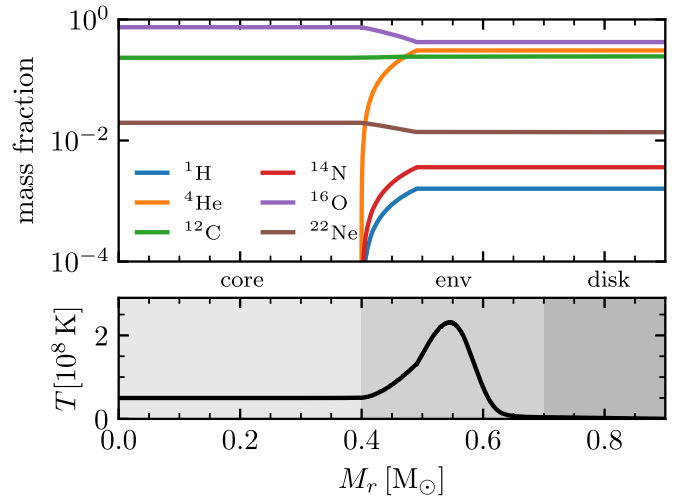

Figure 1. Initial condition representing the immediate post-merger state. The top panel shows the mass fractions of key isotopes; the bottom panel shows the temperature. The three key regions of the remnant are indicated/shaded.

around $M_r = M_{\rm core}$. This initial condition is illustrated in Figure 1. The homogenization of the outer layers is apparent. For example, the surface H layer from the secondary is mixed throughout the envelope/disk region.

2.2. Post-merger to WD Cooling Track

Post-merger, the material near the temperature peak immediately begins to burn. The H is rapidly consumed (within days) and the He first undergoes a flash and then sets up a steady shell-burning structure (in $\sim 10^2$ yr). The H burns through CNO reactions, converting some of the ^{12}C and ^{16}O to ^{14}N. As He burning begins, the reactions $^{14}{\rm N}(\alpha, \gamma)^{18}{\rm F}(\beta^+)^{18}{\rm O}$ and $^{18}{\rm O}(\alpha, \gamma)^{22}{\rm Ne}$ process some of the preexisting and newly generated ^{14}N into neutron-rich isotopes. RCB stars exhibit large $^{18}{\rm O}/^{16}{\rm O}$ ratios (Clayton et al. 2007). Reproducing the ^{18}O and other observed surface abundances provides constraints on the temperature and lifetime of this hot region and the mixing processes that bring this material to the surface (Staff et al. 2012; Menon et al. 2013; Staff et al. 2018; Crawford et al. 2020).

While critical for setting the surface abundances, only $\approx 0.1 \, M_\odot$ of material is processed in the hot, short-lived interface region created in the merger. The overall interior abundance profile is also influenced by the evolution during the extended He-shell-burning phase. Given the presence of a H mass fraction of $X_{\rm H} \sim 10^{-3}$ in the envelope, during He-shell burning the object also has a H burning shell. Because of the small H abundance, this shell is not structurally or energetically important. Because the ^{12}C abundance is much greater than the H abundance, the H is completely consumed in converting the ^{12}C to ^{14}N, increasing the mass fraction of the latter isotope by an amount of $\Delta X_{\rm N} \approx 7 X_{\rm H}$. Then, once this material approaches the temperature of the He-burning shell it is further converted into ^{22}Ne, leading to an enhancement in its mass fraction of $\Delta X_{\rm Ne} \approx 11 X_{\rm H}$. Figure 2 shows a snapshot of the composition profile during the giant phase that illustrates this process.

Because it is not directly observable, the evolution of the interior profile has received less attention than the surface in RCB modeling. Menon et al. (2013), who start with $X_{\rm H} \approx 10^{-2}$ motivated by the thick H envelope on a low-mass He WD secondary, achieve ^{22}Ne fractions $X_{\rm Ne} \approx 10^{-1}$ in accordance with our above estimates (see their Figures 5 and 6).
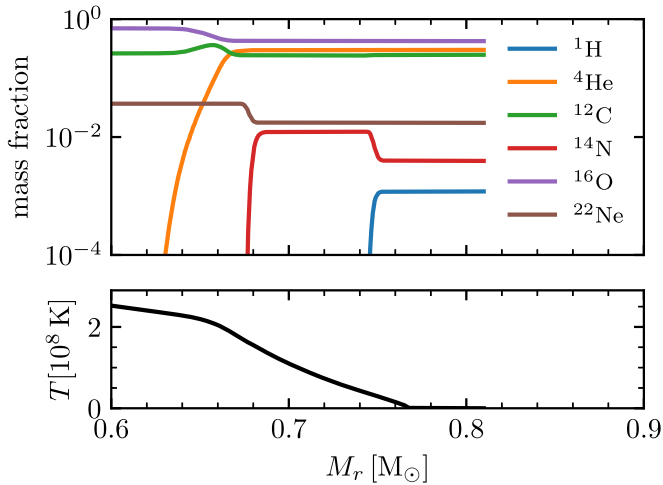
Figure 2. Model during the steady He-shell-burning phase (after ≈ 170 kyr of post-merger evolution). The top panel shows the mass fractions of key isotopes; the bottom panel shows the temperature.
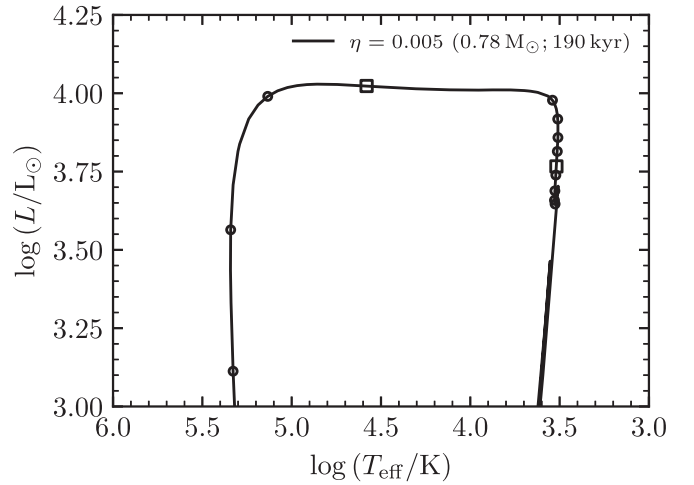

Figure 3. Evolution in the H-R diagram. Along the track, small circles are placed every 20 kyr and large squares every 100 kyr. The legend indicates the assumed mass-loss parameter (using a Bloecker 1995 wind prescription) with the final WD mass and giant phase ($T_{\rm eff} < 10^4$ K) lifetime.
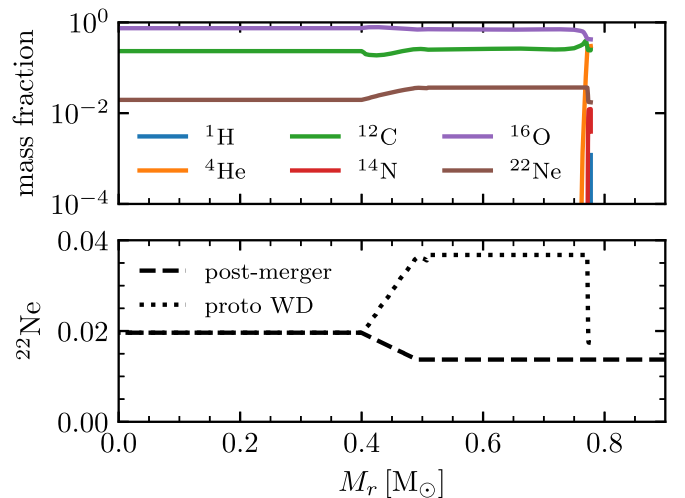

Figure 4. Composition profile when the object is a hot proto-WD. The top panel shows the mass fractions of key isotopes; the bottom panel illustrates the change in the ^{22}Ne abundance profile between this time and the post-merger initial condition shown in Figure 1.

Exactly how much H is present at merger is unclear, and so the predicted ^{22}Ne enhancements are correspondingly uncertain. The H layer masses at the formation of the secondary WD represent an upper limit, as some of this H will be stably transferred in the lead up to the merger (e.g., Kaplan et al. 2012; Shen 2015). Empirically, the observed H abundances in the RCB stars exhibit a large range (Asplund et al. 2000).

Figure 3 shows the evolution in the H-R diagram. The remnant has a cool, luminous giant phase lasting 190 kyr (analogous to the RCB phase) and then has a shorter 10 kyr phase moving blueward (analogous to the EHe phase). This calculation adopts the Bloecker (1995) mass-loss prescription using the parameter $\eta = 0.005$. While this evolution is broadly similar to RCB/EHe stars, the different compositions likely make these observationally distinct. The critical difference from the RCB/EHe stars is that these objects have C/O-dominated surfaces with some He, as opposed to He-dominated surfaces with some C/O. In this case, the abundances of the C/O core of the secondary imply the outer material is expected to be O-rich. This will alter the chemistry of the cool outer layers. The characteristic variability of the RCB star is due to the formation of carbon dust, so these O-rich objects may have different variability properties.

The lower total amount of He present when compared to an RCB star of the same mass suggests a shorter He-shell-burning lifetime. As in the RCB case, a key determinant of the duration of this phase and of the final mass of the WD is the mass-loss rate (Schwab 2019). The mass-loss rates are theoretically uncertain. In AGB stars, the chemistry influences the wind properties (e.g., Höfner & Olofsson 2018), though the extent to which AGB mass-loss rates are appropriate to apply in this circumstance is unclear. If, for example, a lack of carbon dust formation reduces the mass-loss rate relative to mass-loss models calibrated on the C-rich RCB stars, this would lead to longer predicted lifetimes.

If, as a crude estimate, we say that the formation rate of these objects is a factor of ~ 10 lower than for RCB stars due to the requirement for more massive stellar progenitors and the lifetimes are a factor of ~ 3 shorter, then this would suggest ~ 5 galactic objects in this phase relative to the ≈ 150 known RCB stars (e.g., Tisserand et al. 2020). Bauer & Kupfer (2021) estimate that the

Galaxy contains at least $\sim 10^4$ sdB+WD binaries with orbital periods shorter than 1–2 hr, with lifetimes in this phase of ~ 100 Myr. If an order-unity fraction of these objects have an outcome like that discussed in this paper, with remnant lifetimes of ~ 100 kyr, then this too plausibly suggests the Galaxy contains at least ~ 10 merger remnants currently in this phase. On the other hand, the population synthesis results of Zenati et al. (2019) suggest that WD mergers involving a hybrid He/C/O WD could occur at a rate of $\sim 10^{-3}$ yr^{-1} in our Galaxy. With a remnant lifetime of ~ 100 kyr, this would predict as many as ~ 100 galactic objects currently in this phase.

2.3. On the WD Cooling Track

Figure 4 shows the interior composition profile at the time when the object is a hot proto-WD. The object now has a C/O core, and mass loss has reduced the total mass by $\approx 0.1\,M_\odot$. As shown in the bottom panel, the material outside the core has experienced an enhancement in ^{22}Ne mass fraction up to roughly twice its initial

value. During the early phases of the cooling, convection and thermohaline mixing driven by the electron fraction gradient can redistribute this neutron-rich material deeper into the interior (e.g., Brooks et al. 2017; Schwab & Garaud 2019).

Recently, Camisassa et al. (2021) invoked mergers to produce WDs with high ^{22}Ne mass fractions (≈ 0.06) and correspondingly produce significant delays in the WD cooling due to sedimentation heating. Our calculations do find ^{22}Ne enhancement as a result of the merger, with the expected mass fraction effectively determined by the (uncertain) mass fraction of H present in the mixed, post-merger envelope. It is important to note that this level of enhancement is not uniform, but only expected in material processed through the H- and He-burning shells present in the remnant. Thus, the total amount of ^{22}Ne enhancement will also depend on the mass-loss rate of the remnant as this sets the fraction of the envelope material incorporated on the final WD. Given their assumed mass-loss rates, many RCB models find most of the envelope is lost (e.g., Zhang et al. 2014; Lauer et al. 2019; Crawford et al. 2020; Munson et al. 2021), which can then limit the total ^{22}Ne enhancement.

3. Conclusions

We have outlined one future evolutionary pathway for objects in the new class of hot subdwarf–WD binaries described by Kupfer et al. (2020a, 2020b). After evolving to detached WD–WD binaries, gravitational waves will cause these systems to inspiral and their low primary WD masses suggest that they may not suffer a catastrophic thermonuclear explosion at merger. This implies the formation of a long-lived remnant and that their final fate will be a single WD.

The properties of these WD–WD binaries resemble the He WD–C/O WD binaries thought to form the RCB stars and so suggest a similar evolutionary trajectory, though with a few key differences. Because the secondary WD (descended from the hot subdwarf) has already undergone core He burning, the total He supply is reduced (compared to a merger involving a He WD secondary). However, enough He still exists to allow for the formation of a He-shell-burning powered giant star with a C/O-dominated envelope. This giant phase is similar to that of the RCB stars, but with a different envelope composition. Notably, the expectation is that the envelope is O-rich, which may lead to different mass loss and photometric variability properties. In turn, that implies these objects might not be easily detected using techniques optimized for the RCB stars (and their C-rich dust formation events).

The nucleosynthesis that occurs in the post-merger envelope provides a pathway for the enhancement of ^{22}Ne. The amount of ^{22}Ne produced depends on the amount of H incorporated in the post-merger envelope and on the fraction of that envelope that ends up being processed and retained (i.e., not lost to stellar winds). Through their influence on the energy released via gravitational sedimentation and phase separation, these composition differences may manifest as differences in the detailed cooling properties of single WDs produced in mergers. However, additional progress modeling the pre-and-post-merger evolution will be required reliably assess the magnitude of these effects.

Appendix
MESA r12778 Input Physics

The MESA equation of state (EOS) is a blend of the OPAL (Rogers & Nayfonov 2002) SCVH (Saumon et al. 1995) PTEH (Pols et al. 1995), HELM (Timmes & Swesty 2000), and PC (Potekhin & Chabrier 2010) EOSes.

Radiative opacities are primarily from OPAL (Iglesias & Rogers 1993, 1996), with low-temperature data from Ferguson et al. (2005) and the high-temperature, Compton-scattering dominated regime by Buchler & Yueh (1976). Electron conduction opacities are from Cassisi et al. (2007).

Nuclear reaction rates are from JINA REACLIB (Cyburt et al. 2010) plus additional tabulated weak reaction rates (Fuller et al. 1985; Oda et al. 1994; Langanke & Martínez-Pinedo 2000). Screening is included via the prescription of Chugunov et al. (2007). Thermal neutrino loss rates are from Itoh et al. (1996).

ORCID iDs

Josiah Schwab ⓘ https://orcid.org/0000-0002-4870-8855
Evan B. Bauer ⓘ https://orcid.org/0000-0002-4791-6724

References

Asplund, M., Gustafsson, B., Lambert, D. L., & Rao, N. K. 2000, A&A, 353, 287
Bauer, E. B., & Kupfer, T. 2021, arXiv:2106.13297
Bauer, E. B., Schwab, J., & Bildsten, L. 2017, ApJ, 845, 97
Bloecker, T. 1995, A&A, 297, 727
Brooks, J., Schwab, J., Bildsten, L., Quataert, E., & Paxton, B. 2017, ApJL, 834, L9
Buchler, J. R., & Yueh, W. R. 1976, ApJ, 210, 440
Camisassa, M. E., Althaus, L. G., Torres, S., et al. 2021, A&A, 649, L7
Cassisi, S., Potekhin, A. Y., Pietrinferni, A., Catelan, M., & Salaris, M. 2007, ApJ, 661, 1094
Chugunov, A. I., Dewitt, H. E., & Yakovlev, D. G. 2007, PhRvD, 76, 025028
Clayton, G. C. 2012, JAVSO, 40, 539
Clayton, G. C., Geballe, T. R., Herwig, F., Fryer, C., & Asplund, M. 2007, ApJ, 662, 1220
Crawford, C. L., Clayton, G. C., Munson, B., Chatzopoulos, E., & Frank, J. 2020, MNRAS, 498, 2912
Cyburt, R. H., Amthor, A. M., Ferguson, R., et al. 2010, ApJS, 189, 240
Dan, M., Rosswog, S., Brüggen, M., & Podsiadlowski, P. 2014, MNRAS, 438, 14
Ferguson, J. W., Alexander, D. R., Allard, F., et al. 2005, ApJ, 623, 585
Fuller, G. M., Fowler, W. A., & Newman, M. J. 1985, ApJ, 293, 1
Höfner, S., & Olofsson, H. 2018, A&ARv, 26, 1
Hunter, J. D. 2007, CSE, 9, 90
Iglesias, C. A., & Rogers, F. J. 1993, ApJ, 412, 752
Iglesias, C. A., & Rogers, F. J. 1996, ApJ, 464, 943
Itoh, N., Hayashi, H., Nishikawa, A., & Kohyama, Y. 1996, ApJS, 102, 411
Jeffery, C. S. 2008, in ASP Conf. Ser. 391, Hydrogen-Deficient Stars, ed. A. Werner & T. Rauch (San Francisco, CA: ASP), 53
Kaplan, D. L., Bildsten, L., & Steinfadt, J. D. R. 2012, ApJ, 758, 64

Kupfer, T., Bauer, E. B., Burdge, K. B., et al. 2020b, ApJL, 898, L25
Kupfer, T., Bauer, E. B., Marsh, T. R., et al. 2020a, ApJ, 891, 45
Langanke, K., & Martínez-Pinedo, G. 2000, NuPhA, 673, 481
Lauer, A., Chatzopoulos, E., Clayton, G. C., Frank, J., & Marcello, D. C. 2019, MNRAS, 488, 438
Marsh, T. R., Nelemans, G., & Steeghs, D. 2004, MNRAS, 350, 113
Menon, A., Herwig, F., Denissenkov, P. A., et al. 2013, ApJ, 772, 59
Munson, B., Chatzopoulos, E., Frank, J., et al. 2021, ApJ, 911, 103
Neunteufel, P., Yoon, S.-C., & Langer, N. 2016, A&A, 589, A43
Neunteufel, P., Yoon, S.-C., & Langer, N. 2019, A&A, 627, A14
Oda, T., Hino, M., Muto, K., Takahara, M., & Sato, K. 1994, ADNDT, 56, 231
Paxton, B., Bildsten, L., Dotter, A., et al. 2011, ApJS, 192, 3
Paxton, B., Cantiello, M., Arras, P., et al. 2013, ApJS, 208, 4
Paxton, B., Marchant, P., Schwab, J., et al. 2015, ApJS, 220, 15
Paxton, B., Schwab, J., Bauer, E. B., et al. 2018, ApJS, 234, 34
Paxton, B., Smolec, R., Schwab, J., et al. 2019, ApJS, 243, 10
Pols, O. R., Tout, C. A., Eggleton, P. P., & Han, Z. 1995, MNRAS, 274, 964
Potekhin, A. Y., & Chabrier, G. 2010, CoPP, 50, 82
Rogers, F. J., & Nayfonov, A. 2002, ApJ, 576, 1064
Saio, H., & Jeffery, C. S. 2002, MNRAS, 333, 121
Saumon, D., Chabrier, G., & van Horn, H. M. 1995, ApJS, 99, 713
Schwab, J. 2019, ApJ, 885, 27
Schwab, J. 2021, ApJ, 906, 53
Schwab, J., & Garaud, P. 2019, ApJ, 876, 10
Schwab, J., Shen, K. J., Quataert, E., Dan, M., & Rosswog, S. 2012, MNRAS, 427, 190
Shen, K. J. 2015, ApJL, 805, L6
Shen, K. J., Bildsten, L., Kasen, D., & Quataert, E. 2012, ApJ, 748, 35
Shen, K. J., Kasen, D., Miles, B. J., & Townsley, D. M. 2018, ApJ, 854, 52
Staff, J. E., Menon, A., Herwig, F., et al. 2012, ApJ, 757, 76
Staff, J. E., Wiggins, B., Marcello, D., et al. 2018, ApJ, 862, 74
Timmes, F. X., & Swesty, F. D. 2000, ApJS, 126, 501
Tisserand, P., Clayton, G. C., Bessell, M. S., et al. 2020, A&A, 635, A14
Towns, J., Cockerill, T., Dahan, M., et al. 2014, CSE, 16, 62
Townsend, R. 2020, MESA SDK for Linux, 20.3.1, Zenodo, doi:10.5281/zenodo.3706650
van der Walt, S., Colbert, S. C., & Varoquaux, G. 2011, CSE, 13, 22
Webbink, R. F. 1984, ApJ, 277, 355
Wolf, B., Bauer, E. B., & Schwab, J. 2017, wmwolf/MesaScript: A DSL for Writing MESA Inlists, Zenodo, doi:10.5281/zenodo.826954
Wolf, B., & Schwab, J. 2017, wmwolf/py_mesa_reader: Interact with MESA Output, Zenodo, doi:10.5281/zenodo.826958
Zenati, Y., Toonen, S., & Perets, H. B. 2019, MNRAS, 482, 1135
Zhang, X., Jeffery, C. S., Chen, X., & Han, Z. 2014, MNRAS, 445, 660